

Cascade Structured Plasmonic Liquid Crystal Biosensor for the Rapid Detection of Harmful Bacteria Dispersed in Potable Water

Maria Laura Sforza, Francesca Petronella,* Daniela De Biase, Federica Zaccagnini, Seok-In Lim, Usman Akhtar Butt, Antonio d'Alessandro, Nicholas P. Godman, Dean R. Evans, Michael McConney, Kwang-Un Jeong, and Luciano De Sio*

Pathogenic microorganisms contaminating potable water are a serious water quality concern because they have severe consequences for human and environmental health. Managing water contamination requires the availability of fast and highly sensitive point-of-use detection systems responsive to a wide concentration range. In the present work, this goal is achieved by realizing a cascade-structured biosensor that exploits innovative stimuli-responsive materials such as gold nanorods (AuNRs) and photosensitive nematic liquid crystals (NLCs). The cascade structure is fabricated by interfacing a glass substrate in a back-to-front arrangement, hosting an array of bioactivated AuNRs and an NLC cell. The AuNRs array integrates microfluidic channels, allowing direct water sampling and the analysis of reduced water volumes with high sensitivity. The biosensor combines in the same device two independent optical transducers: a bioactive AuNRs array (plasmonic biosensor), sensitive to refractive index alterations, and an NLC cell that detects the presence of pathogens by responding to light intensity variations. The plasmonic biosensor performs exceptionally well for very low concentrations of bacteria. In contrast, the NLC biosensor works for high-concentration bacteria, thus providing a cascade-like detection system able to detect bacteria in a wide concentration range from 10 to 10⁹ CFU mL⁻¹.

1. Introduction

Despite the improvement in the quality of life given by progress and technology, phenomena such as climate change, urbanization, overpopulation, and global traveling connections pose an issue with the spread of infectious diseases in the twenty-first century. They cause outbreaks of new pathogens and re-emerge infections that are considered eradicated,^[1,2] especially if the poor sanitary conditions in many countries worldwide are also considered. While water is essential for life, regrettably, it also serves as one of the most common mediums for pathogen transmission. Responsible management of this fundamental resource requires fast, sensitive, and reliable pathogen detection methods. Although practical, currently used detection methods, such as culture-based processes, polymerase chain reaction (PCR)-based, and


M. L. Sforza, D. De Biase, F. Zaccagnini, U. A. Butt
Department of Medico-Surgical Sciences and Biotechnologies
Sapienza University of Rome
Corso della Repubblica 79, Latina, (LT) 04100, Italy
F. Petronella
National Research Council
Institute of Crystallography CNR-IC
Montelibretti Division
Area territoriale di Ricerca di Roma 1
Strada Provinciale 35d, n. 9, Montelibretti (RM) 00010, Italy
E-mail: francesca.petronella@cnr.it

S.-I. Lim, K.-U. Jeong
Department of Polymer-Nano Science and Technology
Department of Nano Convergence Engineering
Jeonbuk National University
Jeonju 54896, Republic of Korea

A. d'Alessandro
Department of Information Engineering, Electronics and
Telecommunications
Sapienza University of Rome
Via Eudossiana 18, Rome 00184, Italy

N. P. Godman, D. R. Evans, M. McConney
US Air Force Research Laboratory
Wright-Patterson Air Force Base
Dayton, Ohio OH, OH 45433, USA

L. De Sio
Department of Medico-Surgical Sciences and Biotechnologies
Research Center for Biophotonics
Sapienza University of Rome
Corso della Repubblica 79, Latina (LT) 04100, Italy
E-mail: luciano.desio@uniroma1.it

 The ORCID identification number(s) for the author(s) of this article can be found under <https://doi.org/10.1002/adsr.202300201>

© 2024 The Authors. Advanced Sensor Research published by Wiley-VCH GmbH. This is an open access article under the terms of the [Creative Commons Attribution](https://creativecommons.org/licenses/by/4.0/) License, which permits use, distribution and reproduction in any medium, provided the original work is properly cited.

DOI: 10.1002/adsr.202300201

immunology-based procedures, require significant resources and specialized personnel^[3] and must be more suitable for point-of-use detection. Conversely, biosensors are gaining relevance for pathogens detection due to their performance, compactness, and ease of use.^[3] A biosensor is an analytical device that combines a suitable transducer with biological molecules and biochemical reactions to detect chemical/biological compounds by electrical,^[4] thermal,^[5] piezoelectric,^[6] or optical readout.^[7]

Plasmonic nanomaterials and liquid crystals (LCs) have been extensively used in biosensing in separated and combined configurations due to their extraordinary stimuli-responsiveness. Nanotechnology-based biosensors are faster, more sensitive, and more practical than traditional pathogen detection tests because they exploit nanoparticles' unique size and shape-dependent properties.^[8,9] Among different types of nanoparticles (NPs), metallic ones are highly appealing as optical transducers. As described by Ganz's theory,^[10] in metallic NPs, the conduction electrons oscillate when interacting with electromagnetic radiation. This oscillation results in dipoles, giving rise to the localized surface plasmon resonance phenomenon (LSPR). The dipoles oscillate in different directions for each facet of the NP at a resonance frequency determined by the NP chemical composition, size, shape, and surface chemistry. Indeed, for noble metal NPs (Au, Ag, Cu, Pt), the resonance frequency lies in the visible light's wavelength (λ) range.^[11] For this reason, the LSPR phenomenon can be easily detected by observing sharp and intense bands (in the visible λ range) in the absorption spectrum of metallic (plasmonic) NPs.^[12] Moreover, the resonance frequency of the absorption bands depends on the refractive index (n) of the medium surrounding the metallic NP. A change in the medium (e.g., the solvent contamination) gives rise to a change in the n and, therefore, in resonance frequency. Consequently, the LSPR phenomenon of noble metal NPs can be exploited for sensing applications.^[13]

Among noble metal NPs, gold nanorods (AuNRs) are highly appealing for biosensing purposes. The AuNRs anisotropy determines two LSPR frequencies, one associated with the longitudinal oscillations and the other with the transversal ones.^[14] The former produces the longitudinal plasmon band (LPB), and the latter the transverse plasmon band (TPB). While the TPB is usually centered at 520 nm, the LPB can exhibit its maximum value at λ greater than 600 nm, depending on the AuNR's aspect ratio (a parameter linked to the ratio between length and width of the NP). The position of the LPB is sensitive to n variations, thus making AuNRs extremely attractive optical transducers for developing biosensors for pathogens detection.^[15–24]

Other compounds extensively exploited in biosensing applications are LCs.^[25] LCs are optical materials belonging to a state of matter with an organization intermediate between crystals and isotropic liquids, identified as mesophase.^[26] They are elongated organic molecules classified as nematic LCs (NLCs), chiral nematic, blue-phase, and ionic LCs.^[27]

The molecules present a long-range orientational order, described by an order parameter that ranges from 0.3 to 0.8: this value is higher for perfect crystals (≈ 1) and lower for isotropic liquids (≈ 0). The optical birefringence (Δn) and curvature elasticity render LCs remarkably responsive to external influences. This responsiveness to external stimuli and unique properties qualify LCs as reconfigurable materials.^[28] Conse-

quently, LCs are highly esteemed in the materials community for their versatility and adaptability, making them a cornerstone in stimuli-responsive materials.^[29–32] Indeed, in recent years, the ability of LCs to change their molecular orientation (and thus appearance) in the presence of a specific stimulus has proved to be very useful for various applications,^[33–35] including sensing.^[36,37] Biosensors with LCs have been developed for detecting biomarkers,^[38] cells, proteins, biomolecules,^[27,39] and pathogens such as *Salmonella*.^[40] In the latter case, the authors realized an optical transducer designed to induce an alteration of the pitch of a chiral LC (CLC) in the presence of *Salmonella*.

In particular, Janus droplets consisting of a water phase (W) and an organic phase made with a CLC and a fluorocarbon oil (FC-NLC) were prepared and integrated with a purposely synthesized macromolecular surfactant complex functionalized with anti-*Salmonella* antibody (IgG). The molecular surfactant complex lowers the interfacial surface tension as it lays at the W/FC-NLC interface. In the presence of *Salmonella*, the biorecognition with the IgG alters the macromolecular surfactant complex, inducing modulation of the chiral polymer at the W/FC-NLC interface. Consequently, the CLC pitch changes produce a variation of the CLC optical properties, consistent with the *Salmonella* cells' concentration.

In a different approach, other works have demonstrated the increased sensing efficiency of innovative optical transducers that merge plasmonic NPs and LCs. Indeed, NPs, including the gold NPs (AuNPs), can vary the local orientational order parameters of the LCs, mediating the interaction between the biorecognition element and the LCs or behaving as signal amplifiers.^[41]

A biosensor combining AuNPs and LCs was developed to identify DNA hybridization events. The biosensing system exploits the orientation change of LC molecules, occurring upon the increase of DNA molecules in the proximity of the AuNPs surface, caused by hybridization events.^[42]

A similar configuration was exploited to detect human chorionic gonadotropin without false positives,^[43] and a dielectric biosensor was fabricated to detect cardiac troponin I.^[44] In the latter case, AuNPs also behaved as amplifiers of the dielectric signal because, being functionalized with the respective antibody, they caused an accumulation of troponin at the electrode/LCs interface. In addition, the detection of the neurotransmitter acetylcholine was achieved by exploiting the reduction HAuCl_4 induced by the thiocholine, a molecule generated when the enzyme acetylcholinesterase hydrolyzes acetylcholine, its substrate. The formation of AuNPs alters the LC orientation, thus varying the optical signal.^[45]

Although practical and ingenious, these systems still need to be improved as point-of-use devices for their intrinsic complexity.

In the present work, we take a step forward in this field by bridging, in a cascade-like manner, two independent and complementary optical biosensors that exploit the unique properties of an antibody-functionalized AuNRs array integrated with an automatically aligned light-sensitive NLC film. This unique design allows the detection of *Escherichia coli* cells in potable water in a wide concentration range from 10 to 10^9 CFU mL⁻¹. Notably, the integration of microfluidic channels, enabling the manipulation of low volumes of contaminated water, makes the proposed system an effective device for point-of-use water monitoring.

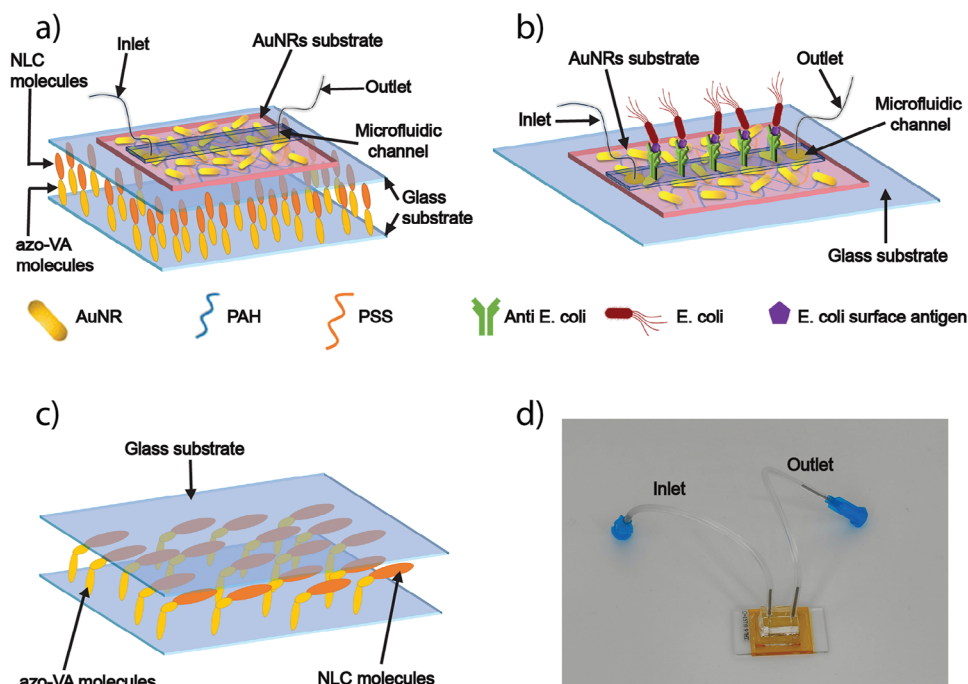


Figure 1. Biosensor consisting of two independent optical components. a) Schematic of the conceived cascade biosensor consisting of two independent components: a glass substrate functionalized with AuNRs, integrating a microfluidic channel, and a glass cell filled with a photoresponsive NLC. b) The area covered by the microfluidic channel is functionalized with an antibody, allowing the spectroscopic recognition of low concentrations of *E. coli* cells c) Schematic of the NLC sample used to detect high concentrations of *E. coli* cells. d) Photo of the realized cascade structured plasmonic/NLC biosensor.

2. Results and Discussion

2.1. Biosensor—Principle of Operation

The biosensor consists of two independent optical components, as schematized in **Figure 1a**. The first component comprises an immobilized AuNRs array functionalized with a polyclonal antibody (anti-*E. coli*, AbE) and integrated with a microfluidic channel. The plasmonic-based optical biosensor underlies the second optical biosensor, a glass cell filled with photo-responsive NLC molecules that are automatically and vertically oriented to respond with an extremely high sensitivity to a variation of a suitable light source.

When water with a low *E. coli* cell concentration (equal to or less than 10^5 CFU mL⁻¹) flows through the microfluidic circuit, the bioactive AuNRs array catches *E. coli* cells, as represented in **Figure 1b**. The univocal interactions between the AbE and the *E. coli* antigen determine an alteration of the n of the medium surrounding the AuNRs array—consequently, the wavelength of the LPB peak red shifts proportionally to the *E. coli* concentration.

The biosensor is conceived so that the underlying NLC biosensor can quantify *E. coli* concentrations equal to or higher than 10^6 CFU mL⁻¹. The photo-responsive NLC cell, represented in **Figure 1c**, is realized so that when the NLC molecules are activated with a suitable (UV) external light source (laser pump), they undergo a reversible orientational transition (from vertical to planar) due to the presence of a minimal concentration of light-sensitive LC (azobenzene molecules) dispersed in conventional NLC. Once water containing a high concentration of *E. coli* bacteria is flown through the microfluidic channel, the intensity of

the pump laser beam is attenuated (*E. coli* bacteria absorb UV light), thus relaxing the NLC molecular orientation (Δn change). Therefore, the Δn variation is proportional to the bacteria concentration. Δn can be easily measured by monitoring the intensity change between parallel/crossed polarizers and measuring the intensity variation of the laser pump transmitted through the NLC cell. Indeed, the device is conceived to provide compactness (as demonstrated in **Figure 1d**) so that the pump laser can also be used as a probe light source.

2.2. Fabrication and Characterization of the AuNRs Array

The AuNRs array was realized by immobilizing AuNRs from a colloidal dispersion on a glass substrate. It was obtained by using the protocol reported in^[21] and^[24] which implies building a PEM by a polyelectrolyte (PE) mediate electrostatic layer-by-layer (eLbL) assembly method and a subsequent immersion step in the AuNRs water dispersion.

Unlike conventional nanofabrication methods, eLbL assembly offers simplicity in reproduction on surfaces of different sizes and geometry, curved or intricately shaped, by merely adjusting solution volumes, immersion duration, and rinsing steps. It allows the deposit of colloidal AuNPs irrespective of their shape. Indeed, they show a surface charge according to their capping agent. To immobilize them on a glass substrate, it is essential to create a suitable PEM, whose final layer should expose a PE with a charge opposite to the surface charge of the NPs. **Figure 2a** illustrates the typical UV–visible absorption spectrum of the AuNRs colloidal dispersion, showing the TPB peak at 512 nm

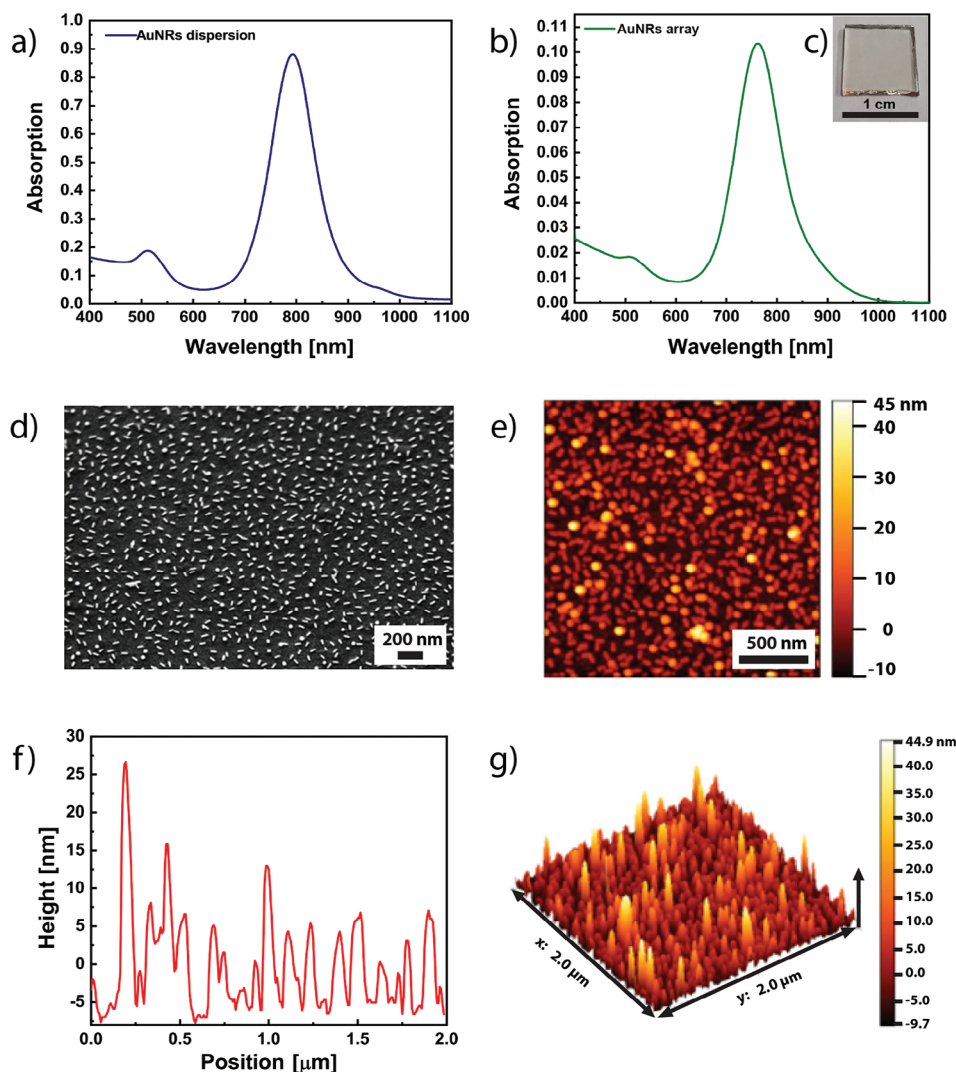


Figure 2. UV–visible spectral properties and morphological analysis of the AuNRs array. a) UV–visible absorption spectrum of AuNRs colloidal dispersion used to realize AuNR array. The characteristic peaks are evident; the transversal plasmon band is centered at 512 nm, and the LPB is at 793 nm. b) UV–visible absorption spectrum of a representative AuNRs array. The peak associated with the LPB is symmetrical, has a FWHM of 108.5 nm, and an absorbance of about 0.1. c) Photograph of the sample after the immobilization of AuNRs by LbL assembly. Note that the rosy color is due to the presence of AuNRs. d) Morphological analysis of the optimized AuNRs array performed by SEM microscopy. The SEM micrograph shows a uniform distribution of the AuNRs with a random orientation. Some AuNRs are vertically oriented and appear as spheres. The fill fraction is 18.33%. e) AFM image of an AuNRs array f) and its AFM line profile. g) 3D AFM topographic reconstruction of the AuNRs array. Images from e–g) confirm the presence of AuNRs and some vertical AuNRs embedded in the PEM.

and the LPB peak at 793 nm. The LPB peak exhibits a full width half maximum (FWHM) of 101 nm. The absorption spectrum of the AuNRs array, as depicted in Figure 2b, reveals distinct LPB and TPB peaks at 762.5 and 506 nm, respectively, with a FWHM of 108.5 nm. Notably, both spectra show symmetric LPB peaks. A comparative analysis of the absorption spectra of the AuNRs' dispersion and AuNRs' array points out that the employed protocol successfully replicates the optical features of AuNRs' colloidal dispersion on a substrate. It is noteworthy that the array's FWHM closely resembles that of the colloidal dispersion, suggesting a uniform distribution of AuNRs and the absence of undesired aggregates. Additionally, as illustrated in Figure 2c, the AuNRs array displays a uniform pinkish hue, typical of AuNRs colloidal

dispersions. These optical findings are consistent with the morphological examination of the AuNRs array. Indeed, the SEM micrograph in Figure 2d shows a uniform and dense distribution of AuNRs, with a fill fraction of 18.33%. The statistical analysis of AuNR dimensions highlights the presence of AuNRs with an average length of 75 ± 19 nm and an average interparticle distance of 51.5 ± 3 nm. Examination of the micrograph also reveals the presence of spherical objects, which correspond to vertically oriented AuNRs within the PEM, a finding corroborated by AFM topographic analysis depicted in Figure 2e. As revealed by AFM, the topography of the AuNRs array showcases anisotropic objects with a height profile ranging between 5 and 20 nm, as illustrated in Figure 2f. Some randomly distributed spherical

asperities, reporting and height between 20 and 30 nm, are also shown. Their topography is consistent with vertically oriented AuNRs, as evidenced by the 3D reconstruction in Figure 2g.

2.3. Fabrication of Microfluidic Platforms and Bioactivation of the AuNRs Array

Microfluidic channels were incorporated into the plasmonic platform to allow the manipulation of small volumes of water, thus minimizing the operator's exposure to a potentially contaminated sample. The master was realized by a print-and-peel xerography process (PPX), detailed in the experimental section. The PPX is fast, inexpensive, and does not require cleanroom facilities or high start-up costs. The channel length was set at 1 cm to fit the dimension of the glass substrate hosting the AuNRs array. As depicted in Figure S1 (Supporting Information), the channel width of 1000 μm was purposely selected to minimize the sticking effect of bacteria cells on the microfluidic channel surface, while the channel nominal thickness is 200 μm . Once applied to the AuNRs substrate, the microfluidic channel was exploited for bioactivating the AuNRs array with the AbE by flowing the AbE solution through the microfluidic channel. The successful AbE incorporation was verified by observing a 45 nm red shift of the LPB peak in the absorption spectrum of the AuNRs array (see Figure S2, Supporting Information for more details).

2.4. Detection of Low *E. coli* Concentrations

The biosensing performance of the proposed system was investigated in a natural water matrix to assess the capability of the device to spectroscopically recognize *E. coli* cells in potable water in a concentration range from 10 to 10^5 CFU mL^{-1} (i.e., in the low concentration range). To this end, the device was filled with artificially contaminated tap water (see experimental section for details) through the inlet of the microfluidic channel (see Figure 1d).

The microfluidic channel was infiltrated with tap water at different *E. coli* concentrations in each biosensing experiment. After the infiltration step, the liquid was left to stand in the channel for 15 min to promote the antigen–AbE interaction. The channel was then rinsed with water, the absorption spectrum recorded, and the microfluidic channel rewashed before the subsequent biosensing experiment was conducted. The difference between the wavelength of the AuNRs LPB peak after and before the contact with the *E. coli* dispersion ($\Delta\lambda$) was calculated for each run. The absorption spectra of each experiment are depicted in Figure 3a–f. The biosensor response was assessed by plotting the $\Delta\lambda$ as a function of the decimal logarithm of *E. coli* concentration, as illustrated in Figure 3g. In this series of experiments, it was observed that $\Delta\lambda$ increases with the rise in *E. coli* concentration. This behavior trend suggests that as the *E. coli* concentration increases in the analyte, the quantity of the antigen–AbE interactions rises, resulting in an increase in the local n and subsequently leading to an elevation of the $\Delta\lambda$ values. This result contrasts our previous findings,^[21] where we demonstrated that $\Delta\lambda$ values decrease with increasing *E. coli* concentration. However, this study utilized a polyclonal AbE to reduce fabrication costs. Polyclonal AbE can bind to different epitopes on the

same antigen, making them more sensitive (albeit less selective than monoclonal antibodies) for biosensing purposes. This increased sensitivity allows for the detection of elevated $\Delta\lambda$ values with increasing *E. coli* concentration. Another drawback of this polyclonal AbE is the increased capacity of non-specific binding. For this reason, it will be replaced with other inexpensive and particular recognition techniques (e.g., synthetic peptides) in future experiments. The experimental points were linearly fitted with the equation:

$$\Delta\lambda = 1.74 (\log_{10} (E.coli)) + 8.85 \quad (1)$$

The details of the linear fit and its parameters are provided in Table S1 (Supporting Information). Additionally, Table S2 (Supporting Information) presents the dataset encompassing experimental points integrated into the fit. Specifically, it details the LPB position post-functionalization with the AbE, the LPB position post-contamination with *E. coli*, the shift ($\Delta\lambda$) of the LPB, and the respective concentration of *E. coli*. The limit of detection (LOD) was calculated as three times the standard deviation of the blank, so it was possible to calculate a LOD of 1 CFU mL^{-1} . The experimental results point out the capability of the proposed microfluidic system to detect *E. coli* cells at low concentrations in tap water, thus demonstrating its suitability as an early detection system able to promptly report the risk of biological contamination of potable water.^[46]

To assess the biosensor's selectivity, it was functionalized with the same antibody (AbE) and tested against a different bacteria strain. In particular, after functionalization with the rabbit polyclonal AbE, the recognition experiments were performed. The functionalization procedure is reported in Section 4. After functionalization, the bioactive array was characterized by the UV-vis spectroscopy technique. The biosensor was then contaminated with *Yersinia ruckeri* (wild type) ATCC29473, a gram-negative bacteria known for causing enteric redmouth disease in some fish species,^[47] at two different concentrations, 10 and 10^2 CFU mL^{-1} . Figure S3a,c (Supporting Information) demonstrate a pronounced red shift of approximately 31 nm following AbE functionalization. Notably, regardless of *Y. ruckeri* concentrations at 10 and 10^2 CFU mL^{-1} , no additional change in the LPB was observed, unequivocally affirming the biosensor's selectivity. This assertion finds reinforced support in Figure S3b,d (Supporting Information), where peak magnifications for 10 and 10^2 CFU mL^{-1} reveal minimal deviation in the LPB position, solidifying the consistency of our findings.

To further demonstrate the proposed plasmonic biosensor's multifunctionality in recognizing other bacteria strains, it was functionalized with a 0.01 mg mL^{-1} water solution of the mouse monoclonal Ab anti-*S. typhimurium* ab8274 (AbS), following the steps detailed in Section 4. After functionalization, UV-vis spectroscopy highlighted a shift of 22 nm in the LPB (Figure S4a, Supporting Information, red curve), proving the correct functionalization with the AbS.

The biosensor was then contaminated with *Salmonella typhimurium* IT2 (SF1), an avirulent laboratory strain of *S. typhimurium*,^[48,49] at a concentration of 10^3 CFU mL^{-1} . Figure S4a (Supporting Information) (green curve) demonstrates an additional redshift of the LPB, extending approximately 23 nm, thus affirming the biosensor's capability to discern diverse bacterial

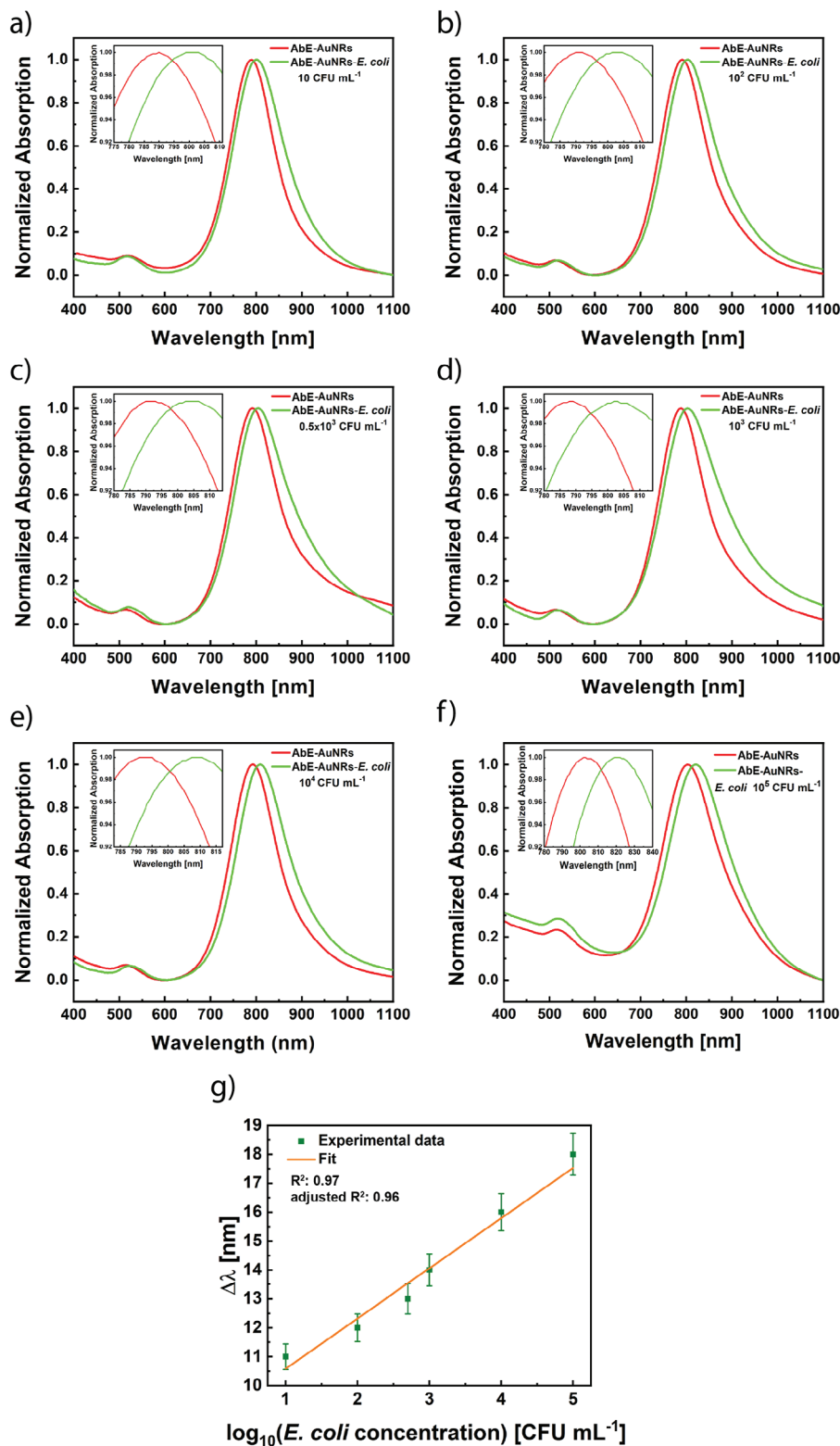


Figure 3. Monitoring of low-range of *E. coli* concentration. Absorption spectroscopy of the AbE-AuNRs array incubated in a) 10, b) 10², c) 0.5 × 10³, d) 10³, e) 10⁴ and f) 10⁵ CFU mL⁻¹ *E. coli* cells dispersion. g) Plot reporting the red-shift values ($\Delta\lambda$) as a function of the decimal logarithm of *E. coli* concentration ranging from 10 to 10⁵ CFU mL⁻¹. The $\Delta\lambda$ values are obtained from the difference of the LPB maximum wavelength measured after incubating the *E. coli* dispersions and the mean value of the LPB maximum wavelength calculated for the AbE-AuNRs array. Experimental data were fitted using Equation 1. It is worth mentioning that for concentrations higher than 10⁵ CFU mL⁻¹, the plasmonic-based biosensor exhibited a loss of sensibility, thus unsuitable for monitoring higher bacteria concentrations.

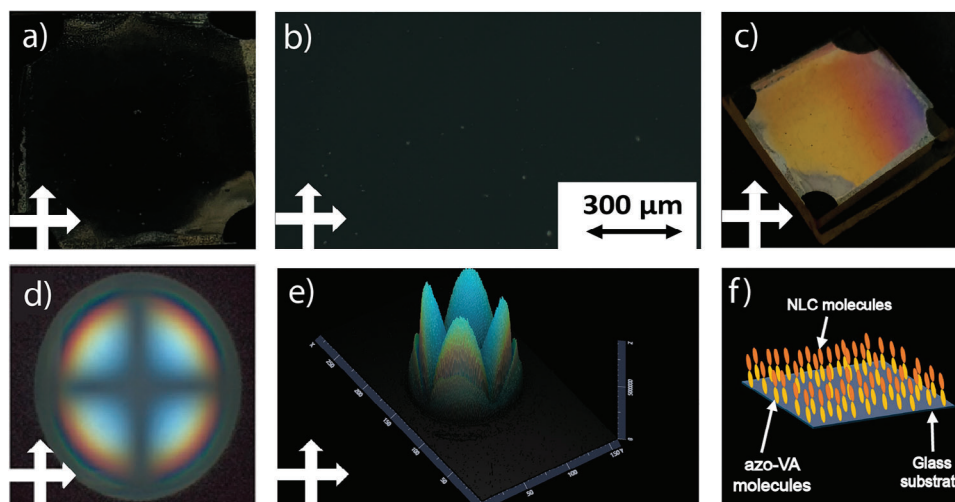


Figure 4. Characterization of the light-responsive NLC sample. a) Polarized photo and b) POM view of the azo-NLC sample. c) Tilted view of the azo-NLC sample between crossed polarizers. d) 2D and e) 3D conoscopic view of the azo-NLC sample that confirms the spontaneous vertical alignment of the azo-NLC molecules. f) Schematic of the vertical alignment of the azo-NLC molecules.

strains. Moreover, Figure S4b (Supporting Information) validates *S. typhimurium* presence through phase contrast microscopy.

2.5. Preparation and Characterization of a Light-Responsive Nematic Liquid Crystal Sample

According to the geometry shown in Figure 1c, a suitably designed NLC cell was incorporated below the AuNRs-based bioactive microfluidic device as a second and additional transduction system to extend the biosensor's operational range. Indeed, as detailed in Section 2.1, the variation of the NLC Δn , i.e., consisting of a slight variation of incident light intensity (I), can be used to detect the presence of *E. coli* cells in water using an optical methodology. For this purpose, a vertically aligned NLC layer was employed to construct the NLC cell. The alignment of the NLC molecules was achieved by utilizing azobenzene molecules (azo-VA) as a photo-alignment material, specifically synthesized to induce self-alignment of the NLC molecules. Subsequently, a 10 μm thick glass cell was infiltrated via capillarity with a mixture comprising azo-VA and the NLC (azo-NLC). The self-alignment of the NLC molecules^[50] was assessed by polarized optical microscopy (POM). The inspection was performed by observing the azo-NLC cell between crossed polarizers using a large acquisition angle and POM in conoscopic mode that integrates a Bertrand lens.

The photo of the azo-NLC cell between cross polarizers is illustrated in Figure 4a, while Figure 4b presents the POM view of the azo-NLC cell sample between crossed polarizers, with the molecular director aligned at 0° relative to the polarizer/analyzer axis. The dark and uniformly observed area in this condition (Figure 4a,b) indicates the consistent vertical alignment of the azo-NLC film. Furthermore, the digital image captured with a tilted view of the azo-NLC cell between cross polarizers exhibited the typical bright area, indicating the vertical alignment of NLC molecules (Figure 4c).^[51] By introducing the Bertrand lenses at the back-focal plane, a dark Maltese cross was observed,^[52] as reported in Figure 4d (2D) and Figure 4e (3D), thus corroborating

the vertical alignment of the NLC molecules, as schematized in Figure 4f.

Figure 5a shows a photo of the sample between crossed polarizers after uniform and homogeneous illumination with a UV lamp (4 mW cm^{-2} at 375 nm for 10 min). The bright area indicates that the *trans-to-cis* isomerization of the azo-VA molecules occurred, producing a planar orientation of the NLC molecules,^[53] as schematized in Figure 5b. Subsequently, the azo-NLC cell was analyzed using the optical setup schematized in Figure 5c. It uses a CW laser ($\lambda = 375 \text{ nm}$), two crossed polarizers, and the azo-NLC cell is placed between the polarizer/analyzer at 45° to respect the polarizer/analyzer axis. The intensity of the light transmitted through the azo-NLC cell (I_t) was collected and measured by a photo-detector placed after the analyzer. This experiment was performed by gradually varying I_0 from 1.316 to 14.474 W cm^{-2} while measuring the corresponding I_t . Experimental results, reported in Figure 5d, indicated that the progressive increase of I_0 produced a sinusoidal-like variation of the I_t . The dependence of I_t from I_0 is in agreement with the following equation:

$$I_t = I_0 * \sin^2 \left(\frac{\pi * \Delta n * d}{\lambda} \right) \quad (2)$$

where I_t is the intensity of the transmitted light, I_0 is the intensity of the laser light impinging the azo-NLC cell, λ is the wavelength of the impinging laser light (375 nm), Δn is the birefringence and d is the thickness of the azo-NLC cell.^[54]

The sinusoidal-like dependence of I_t from I_0 (Figure 5d) agrees with Equation 2. Hence, irradiating the azo-NLC with increasing I_0 values, the NLC molecules progressively change their orientation from vertical to horizontal. The concomitant Δn alteration results in a variation of the I_t . Therefore, the azo-NLC sample works as a phase retarder, thus producing a sinusoidal-like variation (Figure 5d) of the transmitted intensity. The plot in Figure 5d highlights that when I_0 values vary from 1.316 to 6.578 W cm^{-2} , the respective I_t values increase linearly.

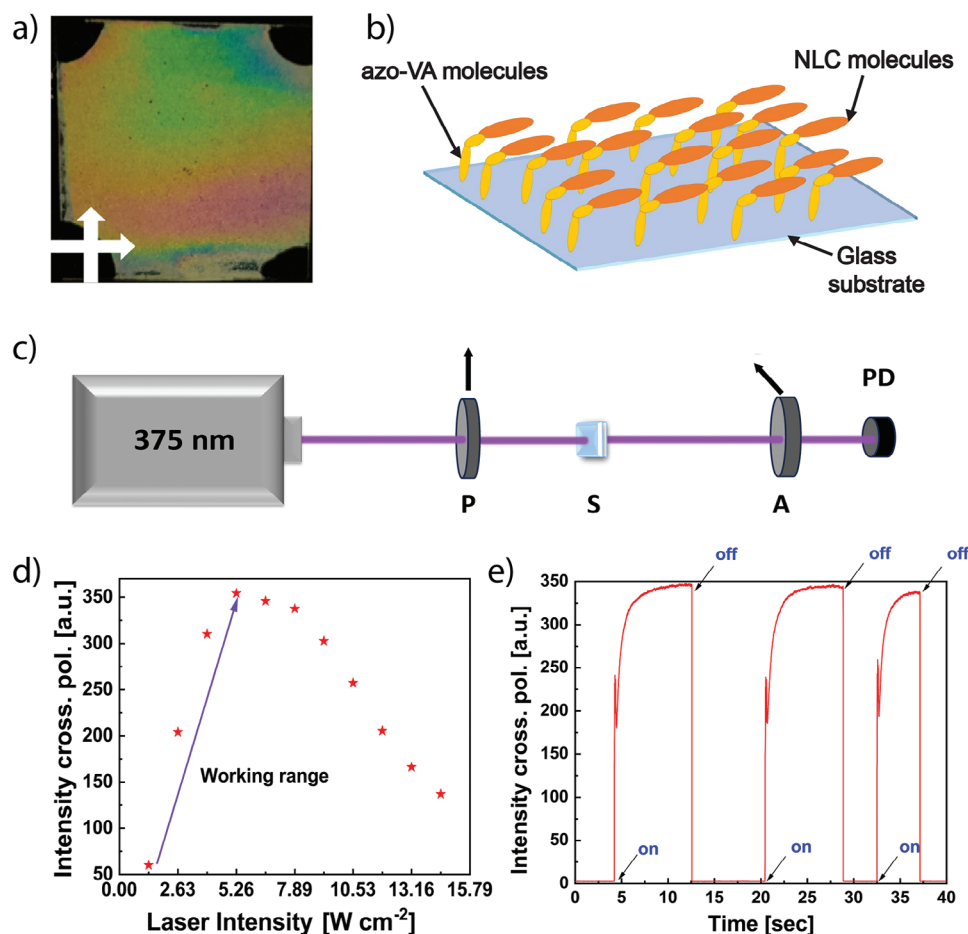


Figure 5. Optical properties of the azo-NLC cell. a) Polarized optical photo of the sample and b) scheme of the planar orientation of the azo-NLC molecules due to the isomerization of azo-VA molecules after illumination with a UV light source ($\lambda = 375$ nm, $I = 4$ mW cm $^{-2}$, $t = 10$ min). c) Optical setup used to study the azo-NLC sample. It uses a CW UV laser source ($\lambda = 375$ nm), a polarizer/analyzer P, A, and a photodetector, PD. d) Transmitted intensity as a function of the incident intensity between crossed polarizers by placing the sample (S) at 45° to the polarizer/analyzer axis. e) Reversible and repeatable changes of the transmitted intensity measured by turning the UV pump/probe beam on and off.

The highest I_0 value of the linear range (6.578 W cm $^{-2}$) was selected as the intensity value of the pump beam in the transmission dynamic experiment to assess the reversibility and repeatability of the azo-NLC molecular transition. The experiment was performed by turning the UV pump/probe beam on and off for three cycles lasting 8 s, 8 s, and 5 s, respectively. The experimental data are reported in Figure 5e and highlighted that the I_t value can be reversibly triggered from low-intensity to high-intensity (pump beam on) and vice versa (pump beam off). This result confirmed the excellent capability of the azo-NLC molecules to be triggered repeatedly from vertical to planar and vice versa in the investigated experimental condition, allowing the reusability of the azo-NLC. As I_t linearly depends on I_0 , in a range from 1.316 to 6.578 W cm $^{-2}$, this range of pump beam intensity was identified as suitable for testing the capability of the azo-NLC cell to detect *E. coli* cells in high concentrations. Indeed, in the biosensor architecture (see Figure 1b), the *E. coli* dispersion that flows through the microfluidic channel induces a decrease of the I_0 according to the *E. coli* concentration. The consequent variation of I_t would indicate the *E. coli* concentration.

A control experiment was performed using pure NLC without adding a small percentage of azo-VA molecules to verify the UV sensitivity introduced by the presence of the azo-VA molecules. To promote the vertical alignment, the NLC was infiltrated inside a commercially available glass cell (10 μ m thick) that induces a homeotropic alignment of the NLC molecules. Figure S5a (Supporting Information) shows a POM view of the sample. It exhibits a uniform vertical alignment, as confirmed by the tilted view photo (Figure S5d, Supporting Information). The sample was then illuminated with a UV light source for different illumination times (Figure S5b–e, Supporting Information, 10 min; Figure S5c–f, Supporting Information, 20 min). Even after 20 min of illumination, the NLC alignment did not show any variation, confirming that the results reported in Figure 5d,e are attributed to the *trans*-to-*cis* isomerization of the azo-VA molecules.

2.6. Detection of High *E. coli* Concentrations

Before assessing the biosensing capability of the azo-NLC cell, absorption spectra of *E. coli* water dispersions at various high

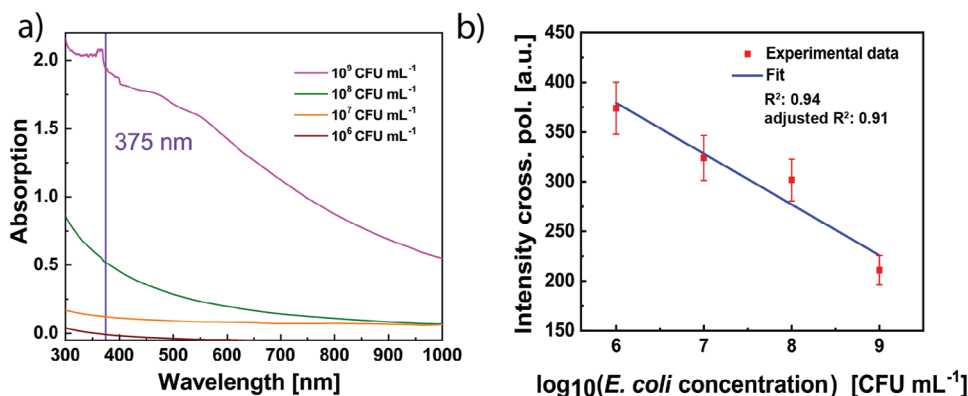


Figure 6. Monitoring of high-range of *E. coli* concentration. a) Absorption spectra of the *E. coli* water dispersions at different high concentration levels. b) Linear fit (blue line) of the transmitted intensity experimental data as a function of the decimal logarithm of *E. coli* concentration ranging from 10^6 to 10^9 CFU mL $^{-1}$.

concentration levels (ranging from 10^6 to 10^9 CFU mL $^{-1}$) were obtained and are presented in **Figure 6a**. The spectra highlight a notable alteration in absorption intensity below 500 nm, with a particularly pronounced change observed at 375 nm (the wavelength of the laser pump). This change can be attributed to the intrinsic absorption/scattering characteristics of the *E. coli* cells.^[55,56]

These results confirm that the wavelength of 375 nm is suitable both as a trigger of the NLC transitions (pump) and as a probe (once the beam is transmitted through the azo-NLC cell) to determine the bacteria concentration by measuring its intensity between cross polarizers (see **Figure 5a**). Remarkably, this set of experiments was performed by directly dispersing *E. coli* cells in tap water and using the device shown in **Figure 1d**.

The *E. coli* dispersion flows through microfluidic channels incorporated into the bioactive AuNRs array, which is sealed at the azo-NLC cell. The pump laser irradiates the microfluidic channel, which is set at the intensity $I_0 = 6.578$ W cm $^{-2}$.

The *E. coli* cells absorb photons from the laser pump beam, decreasing the laser pump's intensity value (I_0) and impinging the azo-NLC cell. Such a decrease induces changes in the NLC Δn . Consequently, the transmitted intensity between crossed polarizers (I_t) varies. The plot in **Figure 6b**, reporting the I_t as a function of *E. coli* concentration, evidences a linear correlation between the *E. coli* concentration and the I_t according to the following equation:

$$I_t = -51.16 (\log_{10} (E. coli \text{ concentration})) + 686.34 \quad (3)$$

where I_t is the transmitted intensity.

As such, it is possible to correlate the I_t to the *E. coli* bacteria concentration, thus producing a novel methodology for monitoring high bacteria concentration with high precision using a light-sensitive NLC. The details of the linear fit are provided in **Table S3** (Supporting Information). Noteworthy is that the azo-NLC biosensor provides only a quantitative measurement without a qualitative evaluation because it works independently from the plasmonic biosensor, so it does not rely on specific receptors that can recognize the *E. coli* bacteria in a particular manner. However, once the specific bacteria strain is identified using the

plasmonic biosensor, the azo-NLC one allows continuous monitoring of high bacteria concentrations.

A control experiment was conducted to confirm that the I_t variation is associated with the azo-NLC molecule's light sensitivity. The azo-NLC cell was irradiated by the pump beam laser with the highest intensity of the laser (14.474 W cm $^{-2}$) for 2 minutes. During the irradiation, the temperature was measured using a high-resolution thermal camera. The resulting thermographic analysis reported in **Figure S6** (Supporting Information) showed a negligible temperature increase under the investigated experimental conditions. Accordingly, the azo-NLC reorientation is caused by a light stimulus, not a thermal one.

3. Conclusion

In this work, we have reported an innovative plasmonic and NLC-based biosensor for detecting harmful bacteria in potable water. The biosensor, equipped with microfluidic channels, can analyze the reduced volume of water by exploiting the localized surface plasmon resonance phenomenon of AuNRs and the photo-responsive properties of azo-NLCs. The longitudinal plasmon band (LPB) resonance wavelength of an array of AuNRs is affected by their surrounding medium's refractive index. Therefore, a variation of the refractive index, such as bacteria contamination, is recorded by monitoring the spectroscopic shift of the LPB peak wavelength. Functionalizing the AuNRs array with a polyclonal antibody anti *E. coli* made it possible to selectively detect low concentrations of *E. coli* cells in water between 10^4 and 10^5 CFU mL $^{-1}$. The presence of a light-sensitive azo-NLC also makes the biosensor sensitive to high concentrations of *E. coli* cells. NLCs modified with azobenzene (azo-NLC) rapidly change the orientation of their molecules when irradiated with UV light due to the cis-trans isomerization of azobenzene and promptly results in the presence of brightness when observing the azo-NLC with crossed polarizers. The change in orientation also affects the transmitted intensity, which assumes a sinusoidal-type variation. The presence of the bacteria alters the transmitted intensity. It allows the detection of concentrations of *E. coli* cells from 10^6 to 10^9 CFU mL $^{-1}$, exploiting the linear range of the transmitted intensity. Therefore, the biosensor can quickly detect

bacteria from low (from 10 to 10⁵ CFU mL⁻¹) to high (from 10⁶ to 10⁹ CFU mL⁻¹) concentrations.

To evaluate the selectivity of the proposed biosensor, we subjected the AuNRs array functionalized with the same polyclonal antibodies targeting *E. coli* to contamination with a distinct bacterial strain (*Y. ruckeri*). This contamination was carried out at varying concentrations of 10 and 10² CFU mL⁻¹. However, in both instances, no bacterial presence was detected, thereby affirming the biosensor's selectivity. The biosensor's versatility was confirmed by functionalizing it with an anti-*S. typhimurium* antibody, followed by contamination with *S. typhimurium* at a concentration of 10³ CFU mL⁻¹. This experiment successfully demonstrated the biosensor's capability to recognize other bacterial strains, showcasing its adaptability for detecting various pathogens in drinkable water. Future investigations will center on enhancing the sensitivity of the azo-NLC biosensor through adjustments to geometrical and physical parameters, such as cell thickness and azo-VA concentration.

These findings have paved the way for a new generation of early warning multi-component systems capable of swiftly detecting harmful microbes dispersed in drinkable water across a spectrum of concentrations.

4. Experimental Section

Materials: Glass slides were purchased from Menzel Gläser. Citrate capped gold nanorods (AuNRs 55 nm × 15 nm, O.D. 50) were purchased from Nanocomposix, poly(sodium 4-styrenesulfonate) (PSS, *M_w* 70 000 Da), poly(allylamine hydrochloride) (PAH, *M_w* 50 000 Da), acetone, isopropanol, and methanol and sodium chloride were purchased from Merck. Rabbit polyclonal anti-*E. coli* NB-47-00442 was purchased by NE-Biotech, *E. coli* K12 strain MG1655 was obtained from the CGSC (Coli Genetic Stock Centre) collection, and chemical minimal medium for the growth of bacteria were purchased from Merck or VWR international. For the water-soluble azobenzene, potassium carbonate (K₂CO₃, 99%), anhydrous magnesium sulfate (MgSO₄, 99.5%), acetone, chloroform, hexane, methanol, and ethyl acetate were purchased from Showa. 1-Methyl-imidazole was purchased from Sigma-Aldrich, and NLC E7 was purchased from Merck. Sylgard 184 Silicone Elastomer KIT was purchased from Farnell. Millipore water (MilliQ or water) was used to prepare the AuNR dispersion; the PE solutions, the antibody dilution, and the washing steps were not specified. For the synthesis of the azo-VA: 4-hydroxy-4'-dimethylaminoazobenzene (98%, TCI), 6-bromo-1-hexanol (95%, TCI), acryloyl chloride (98%, Sigma), potassium carbonate (K₂CO₃, 99%, Showa), potassium iodide (KI, 99%, Showa), triethyl amine (98%, Sigma), sodium sulfate (Na₂SO₄, 99%, Showa), methanol (99%, Samchun), 2-butanone (99%, Samchun), chloroform (CHCl₃, 99%, Samchun), dichloromethane (DCM, 99%, Samchun) were purchased and used without further purification.

Synthesis of Photoresponsive LCs (azo-NLC): Azo-VA was synthesized in two steps:

(1): Azo-OH

4-Hydroxy-4'-dimethylaminoazobenzene (1.0 g, 4.14 mmol) and 6-bromo-1-hexanol (1.65 mL, 4.97 mmol) were dissolved in 150 mL of 2-butanone, and then K₂CO₃ (1.14 g, 8.28 mmol) and KI (0.068 g, 0.414 mmol) were added to the above solution. The resulting solution was refluxed at 70 °C for 48 h. After that, the resulting solution was filtered and evaporated. After evaporating solvents, the resultant solid was extracted thrice with CHCl₃ and distilled water. After drying the organic layer over sodium sulfate (Na₂SO₄), the crude solid was obtained by evaporating the solvent. The crude solid was dissolved in 5 mL of methanol and 200 mL of water was poured to precipitate the product. Finally, the prod-

uct was collected and dried in a vacuum oven for 24 h. (yield: 80%). ¹H NMR (500 MHz, CDCl₃): δ = 1.44-1.65 (m, 6H), 1.80-1.86 (m, 2H), 3.08 (s, 6H), 3.64-3.69 (t, 2H), 4.02-4.06 (t, 2H), 6.74-6.77 (d, 2H), 6.95-6.98 (d, 2H), 7.81-7.85 (m, 4H)

(2): Azo-VA

The solution of acryloyl chloride (0.265 g, 2.93 mmol) in 30 mL of DCM was slowly added dropwise to a solution of Azo-OH (0.5 g, 1.46 mmol) and triethylamine (0.148 g, 1.46 mmol) in 50 mL of DCM at 0 °C for about 1 h. Subsequently, the reaction mixture was stirred for 48 h at room temperature. The K₂CO₃ solution was added to the resulting solution and extracted with DCM three times. The solvent evaporated after drying the organic layer over Na₂SO₄, and the crude solid was obtained. The crude solid was dissolved in 5 mL of methanol and poured 200 mL of water to precipitate the product. Finally, the product was collected and dried in a vacuum oven for 24 h. (yield: 70%). ¹H NMR (500 MHz, CDCl₃): δ = 1.50-1.54 (m, 4H), 1.69-1.75 (m, 2H), 1.80-1.86 (m, 2H), 3.1 (s, 6H), 4.01-4.04 (t, 2H), 4.14-4.19 (t, 2H), 5.80-5.83 (m, 1H), 6.09-6.15 (m, 1H), 6.37-6.42 (m, 1H), 6.74-6.77 (d, 2H), 6.95-6.98 (m, 2H), 7.80-7.85 (m, 4H).

A schematic summary of the synthesis, the ¹H NMR spectra of Am-Azo-OH and Am-Azo-acrylate, UV-vis absorption spectra of Am-Azo-acrylate and a schematic procedure for the fabrication of azobenzene-attached glass substrate are reported in Figure S7 (Supporting Information).

Bacteria Culture: The reference *E. coli* laboratory strain used in this study is *E. coli* K12 strain MG1655 (*E. coli*). The chemically defined media, minimal medium A or minimal medium E supplemented with 0.2% and 0.4% glucose, respectively, were used in this study to grow *E. coli*. Briefly, a few colonies of *E. coli* from a freshly streaked plate were transferred into 30 mL of chemically defined medium in a 250 mL Erlenmeyer flask and allowed to grow overnight at 37 °C under orbital shaking. The culture was centrifuged at 8000 g for 15 min, the spent medium was discarded, and the bacterial pellet was resuspended in 20 mL of a physiological solution (0.9% NaCl). The growth of *E. coli* was monitored by determining the optical density at 600 nm (OD₆₀₀). The optical density was measured, and an aliquot of the bacteria was further diluted in the growth medium to 10⁷ CFU mL⁻¹.

Fabrication of Gold Nanorods Arrays: AuNR arrays were fabricated by optimizing the protocol described in refs.[21, 24] A glass slide was cut, obtaining 1 cm × 1 cm substrates cleaned by sequential sonication in methanol and acetone with an intermediate rinsing step in isopropanol.

After that, the sequence of PEs PAH/PSS/PAH (or PE multilayer, PEM) was assembled on the glass substrate. PAH and PSS solutions 1.6 mg mL⁻¹ were used, and MilliQ was used in the rinsing step. First, the substrate was immersed in PAH for 10 min, followed by immersion in water for 2 min to remove excess PAH. Then, substrates were immersed in the PSS solution for 10 min, rinsed with water, and immersed in PAH. Finally, substrates were rinsed for 2 min with water, followed by a stream of nitrogen to dry them. AuNRs were immobilized on the PEM-functionalized substrates by immersing them in a water dispersion of AuNRs with an optical density of 0.8 (at 790 nm) for 16 h. After the immersion, the resulting AuNR arrays were washed with water, dried with a nitrogen stream, and characterized.

Fabrication of Microfluidic Channels: Low-resolution microfluidic channels were realized using a master prepared by the print-and-peel xerography process (PPX). It has been recognized as a convenient prototyping technique suitable for academic settings. Indeed, the PPX is fast, inexpensive, and does not require cleanroom facilities or high start-up costs.

The PPX started with selecting the Kapton as a suitable adhesive tape, having a nominal thickness of 50 μm. The overlapping of 4 layers of this tape led to a height of 200 μm, corresponding to the desired one for the microfluidic circuit. First, the tape adhered to a glass substrate incorporated into a circuit cutting mat and introduced in the cutting plotter (BlackHole Lab Cutting Machine). Next, the desired pattern was realized using the property software "Circuit Design Space." The pattern was set up to print the PPX master with a thickness of 200 μm and a width of 1000 μm. The xerography plotter was activated to transfer the desired

pattern to the Kapton tape on the glass substrate. At this stage, the tape-on-glass was withdrawn from the plotter and washed by immersion in isopropanol (20 min) to facilitate the removal of excess tape. The resulting master consisted of 4 Kapton layers with a specific geometry on the glass substrate.

The replica molding process was utilized to realize the polydimethylsiloxane (PDMS) channel fabrication. To this end, the PDMS (Dow Corning Sylgard 184) was prepared by mixing the monomer and the catalyst in a ratio of 10:1. The mixture was carefully stirred and then gradually degassed in a vacuum chamber until all the air bubbles were removed. At this stage, the master, previously accommodated inside a Petri dish, was introduced into the vacuum chamber, and the PDMS mixture was carefully poured on. After a further degassing step, the system was cured in an oven preheated at 80 °C for 40 min. Then, the PDMS microfluidic channel was released from the mold, carefully rinsed with isopropanol, and analyzed by the optical microscope, as reported in Figure S1 (Supporting Information).

Fabrication of the Azo-Nematic Liquid Crystal Cell: To fabricate the azo-NLC cell, a mixture containing the E7 NLC and the azo-VA molecules (in a weight ratio of 98:2) was prepared and stirred at 30 °C for 15 min. Next, the glue NOA 61 with 10 μm glass microbeads was deposited on the corners of a glass substrate. After that, a second glass top substrate was placed on the first one, and the cell was sealed by irradiation with UV light for 1 min. Finally, the resulting glass cell was infiltrated by capillary effect with the azo-NLC mixture and used for further experiments.

Assembly of the Device: The AuNRs array and the microfluidic PDMS chamber were placed in a plasma chamber and exposed to oxygen plasma for 1 min at 900 mW. Subsequently, the two parts were brought into contact and permanently bonded. For incorporating the azo-NLC cell, the AuNRs array, integrating the microfluidic chamber and the azo-NLC cell, were glued using NOA-61 photopolymer.

Functionalization of the AuNRs Array with the Antibody: A 0.08 mg mL⁻¹ water solution of the rabbit polyclonal antibody (Ab) anti *E. coli* (AbE) NB-47-00442 was introduced into the microfluidic channel. After 90 min, the AbE solution was removed, and water was allowed to flow through the channels to remove the AbE excess, unbound to the AuNRs array. After functionalization, the bioactive array was characterized with UV–vis spectroscopy and used for the experiments.

Optical Properties of the Azo-NLC Sample: A 10 μm tick glass cell was infiltrated with the azo-NLC using a capillary filling. To study the self-alignment of the azo-NLC molecules, the glass cell was inspected between crossed polarizers utilizing a POM technique in conoscopic mode that integrates a Bertrand lens. For this purpose, the Zeiss Axiolab 5 Polarizing Microscope was used. To investigate the optical response of the sample under suitable laser illumination, a pump/probe optical setup was realized using a solid-state OBIS CW UV laser source ($\lambda = 375$ nm), a polarizer before the sample and an analyzer after it. Signals were collected using a photodetector, the PDA8A2-Si Fixed Gain Detector (320–1000 nm, 50 MHz BW) from Thorlabs. The sample was placed at 45° to the polarizer/analyzer (P/A) axis. After gradually increasing the laser intensity from 0 to 14.474 W cm⁻² and analyzing the behavior of azo-NLC molecules, the pump/probe beam was turned on and off at the highest intensity (6.579 W cm⁻²) of the linear range to test the reversibility and repeatability of the azo-NLC molecules transition. Indeed, the linear range was identified for testing the azo-NLC sample to monitor high bacteria concentrations.

Biosensing of *E. coli* Dispersions: The biosensing performance of the device was investigated in a real water matrix. For analyzing low-concentration *E. coli* water dispersions, a defined volume (9 mL) of potable tap water was withdrawn. Then, 1 mL of *E. coli* cells (10⁵ CFU mL⁻¹, dispersed in NaCl 0.155 M) was added to reach a final concentration of 10⁴ CFU mL⁻¹ in tap water. This 10⁴ CFU mL⁻¹ tap water dispersion was used by sequential dilutions to prepare four tap water *E. coli* dispersions in a concentration range from 10 CFU mL⁻¹ to 10³ CFU mL⁻¹. At this stage, the device was infiltrated through the inlet with *E. coli* dispersed in tap water at five different concentrations and let unperturbed for 15 min to allow the antibody to recognize and catch *E. coli* cells from the water dispersion.

After a rising step, performed by fluxing water, the sample was let to dry before measuring its absorption spectrum. Absorption spectroscopy

measurements were carried out using an optical setup equipped with an absorption fiber-coupled spectrophotometer that probes an area of the sample precisely in correspondence with the microfluidic channel.

The biosensor response was evaluated by plotting the $\Delta\lambda$ (defined as the difference between the wavelength of the LPB peak after and before the contact with *E. coli* dispersion) as a function of the *E. coli* concentration.

For analyzing highly concentrated *E. coli* water dispersions, 1 mL of a 10⁹ CFU mL⁻¹ *E. coli* sample was collected by centrifugation, dispersed in tap water, and used for preparing, by sequential dilution, three dispersions with a concentration of 10⁸, 10⁷, and 10⁶ CFU mL⁻¹ respectively. The absorption spectrum of each dispersion was measured. The biosensing device introduced in the optical setup (Figure 5c) was activated by turning on the pump/probe laser (OBIS CW UV laser source ($\lambda = 375$ nm)). Subsequently, the microfluidic channel was infiltrated with *E. coli* dispersions at different concentrations. The photodetector monitored the consequent intensity variation. A rinsing step was performed before infiltration the subsequent *E. coli* dispersion by flowing a NaCl 0.1 M solution.

UV–Visible Spectroscopy: UV–visible absorption spectroscopy was performed using a USB spectrophotometer (USB 2000 + XR1, Ocean Optics, FL, USA). A diode array spectrophotometer HP8453 (Agilent Technologies) was used to measure the OD₆₀₀ of *E. coli* cell cultures.

Scanning Electron Microscopy: To investigate the morphology of the AuNR arrays, scanning electron microscopy (SEM) micrographs were obtained using a high-resolution scanning electron microscope (AURIGA from Zeiss). Measurements were performed at the interdepartmental research center on nanotechnologies applied to engineering (C.N.I.S. - Sapienza University of Rome).

Atomic Force Microscopy: Atomic force microscopy (AFM) was used to investigate the surface profile of AuNR arrays. Measurements were performed at the interdepartmental research center on nanotechnologies applied to engineering (C.N.I.S.-Sapienza University of Rome) using the AFM Veeco Icon and the AFM Veeco Multimode.

Photothermal Characterization: A control experiment was conducted to show that the observed phenomenon is associated with the NLC molecules' light sensitivity. By irradiating the sample for 2 min with the highest intensity (14.474 W cm⁻²) of the solid-state OBIS laser operating at 375 nm, the temporal temperature variation was recorded using a high-resolution thermal camera (FLIR, A655sc). The thermal images have 640×640 pixels with an accuracy of ±0.2 °C. The data were acquired and processed using the FLIR ResearchIR Max software.

Statistical Analysis: The UV–vis absorption spectra were standardized between 0 and 1 using OriginLab software. This software also facilitated the statistical analysis of both spectroscopic and photothermal data. The efficacy of the weighted linear fits was assessed by determining R^2 and adjusted R^2 coefficients. ImageJ software was employed to statistically analyze the SEM micrographs, providing a robust analytical framework.

Supporting Information

Supporting Information is available from the Wiley Online Library or from the author.

Acknowledgements

This work was fully supported by the “NATO – Science For Peace and Security Programme (SPS-G5759, NANO-LC).”

Conflict of Interest

The authors declare no conflict of interest.

Data Availability Statement

Research data are not shared.

Keywords

biosensors, liquid crystals, pathogens, plasmonics, water

Received: December 15, 2023

Revised: April 17, 2024

Published online:

- [1] R. E. Baker, A. S. Mahmud, I. F. Miller, M. Rajeev, F. Rasambainarivo, B. L. Rice, S. Takahashi, A. J. Tatem, C. E. Wagner, L.-F. Wang, A. Wesolowski, C. J. E. Metcalf, *Nat. Rev. Microbiol.* **2022**, *20*, 193.
- [2] C. Mora, T. Mckenzie, I. M. Gaw, J. M. Dean, H. Von Hammerstein, T. A. Knudson, R. O. Setter, C. Z. Smith, K. M. Webster, J. A. Patz, E. C. Franklin, *Nat. Clim. Change* **2022**, *12*, 869.
- [3] J. Li, Y. Zhu, X. Wu, M. R. Hoffmann, *Clin. Infect. Dis.* **2020**, *71*, S84.
- [4] K. G. Gunasinghe Pattiya Arachchillage, S. Chandra, A. Williams, S. Rangan, P. Piscitelli, L. Florence, S. Ghosal Gupta, J. M. Artes Vivancos, *Biosens. Bioelectron.* **2023**, *239*, 115624.
- [5] F. Narita, Z. Wang, H. Kurita, Z. Li, Y. Shi, Y. Jia, C. Soutis, *Adv. Mater.* **2021**, *33*, 2005448.
- [6] Z. Zhang, Q. Wang, L. Han, S. Du, H. Yu, H. Zhang, *Sens. Actuators, B* **2018**, *268*, 188.
- [7] F. Baldini, M. Minunni, *Anal. Bioanal. Chem.* **2019**, *411*, 7605.
- [8] N. Sanvicens, C. Pastells, N. Pascual, M.-P. Marco, *TrAc, Trends Anal. Chem.* **2009**, *28*, 1243.
- [9] H. Zhang, X. Liu, M. Liu, T. Gao, Y. Huang, Y. Liu, W. Zeng, *Biosens. Bioelectron.* **2018**, *99*, 625.
- [10] J. Cao, T. Sun, K. T. V. Grattan, *Sens. Actuators, B* **2014**, *195*, 332.
- [11] J. Z. Wu, S. A. Ghopry, B. Liu, A. Shultz, *Micromachines* **2023**, *14*, 1393.
- [12] L. De Sio, in *Active Plasmonic Nanomaterials*, Pan Stanford Publishing, Singapore, **2015**, Chaps. 1 and 7.
- [13] P. K. Jain, M. A. El-Sayed, *J. Phys. Chem. C* **2007**, *111*, 17451.
- [14] L. M. Liz-Marzán, *Mater. Today* **2004**, *7*, 26.
- [15] S. Mahari, A. Roberts, S. Gandhi, *Food Chem.* **2022**, *390*, 133219.
- [16] F. Petronella, M. De Angelis, D. DeBiase, S.-I. Lim, K.-U. Jeong, N. Godman, D. Evans, M. Mcconney, L. De Sio, in 2021 IEEE 8th Int. Workshop on Metrology for AeroSpace (MetroAeroSpace), IEEE, Piscataway, NJ **2021**, p. 469.
- [17] N.-S. Eum, S.-H. Yeom, D.-H. Kwon, H.-R. Kim, S.-W. Kang, *Sens. Actuators, B* **2010**, *143*, 784.
- [18] X. Li, L. Jiang, Q. Zhan, J. Qian, S. He, *Colloids Surf., A* **2009**, *332*, 172.
- [19] S. Kaushal, N. Priyadarshi, A. K. Pinnaka, S. Soni, A. Deep, N. K. Singhal, *Sens. Actuators, B* **2019**, *289*, 207.
- [20] F. Yaghubi, M. Zeinoddini, A. R. Saeedinia, A. Azizi, A. Samimi Nemati, *Plasmonics* **2020**, *15*, 1481.
- [21] F. Petronella, D. De Biase, F. Zaccagnini, V. Verrina, S.-I. Lim, K.-U. Jeong, S. Miglietta, V. Petrozza, V. Scognamiglio, N. P. Godman, D. R. Evans, M. Mcconney, L. De Sio, *Environ. Sci.: Nano* **2022**, *9*, 3343.
- [22] Y. J. Choi, J. U. Lee, S. J. Sim, *Sens. Actuators, B* **2022**, *350*, 130880.
- [23] L. P. F. Peixoto, J. F. L. Santos, G. F. S. Andrade, *Anal. Chim. Acta* **2019**, *1084*, 71.
- [24] F. Zaccagnini, P. Radomski, M. L. Sforza, P. Ziótkowski, S.-I. Lim, K.-U. Jeong, D. Mikielawicz, N. P. Godman, D. R. Evans, J. E. Slagle, M. E. Mcconney, D. De Biase, F. Petronella, L. De Sio, *J. Mater. Chem. B* **2023**, *11*, 6823.
- [25] Z. Wang, T. Xu, A. Noel, Y.-C. Chen, T. Liu, *Soft Matter* **2021**, *17*, 4675.
- [26] E. Priestly, in *Introduction to Liquid Crystals*, 1975th ed. (Eds: E. B. Priestley, P. J. Wojtowicz, P. Sheng), Springer, New York **2012**, p. 1.
- [27] R. Qu, G. Li, *Biosensors* **2022**, *12*, 205.
- [28] S. Bahl, H. Nagar, I. Singh, S. Sehgal, *Mater. Today* **2020**, *28*, 1302.
- [29] H. K. Bisoyi, Q. Li, *Chem. Rev.* **2022**, *122*, 4887.
- [30] Y.-K. Kim, J. Noh, K. Nayani, N. L. Abbott, *Soft Matter* **2019**, *15*, 6913.
- [31] M. Liu, S. Yang, *Acc. Chem. Res.* **2024**, *57*, 739.
- [32] M. del Pozo, J. A. H. P. Sol, A. P. H. J. Schenning, M. G. Debije, *Adv. Mater.* **2022**, *34*, 2104390.
- [33] W.-K. Fong, T. Hanley, B. J. Boyd, *J. Controlled Release* **2009**, *135*, 218.
- [34] Y. Choi, D. Choi, J.-K. Choi, K.-S. Oh, E. Cho, J.-H. Im, D. P. Singh, Y.-K. Kim, *ACS Appl. Opt. Mater.* **2023**, *1*, 1879.
- [35] F. Petronella, T. Madeleine, V. De Mei, F. Zaccagnini, M. Striccoli, G. D'alessandro, M. Rumi, J. Slagle, M. Kaczmarek, L. De Sio, *ACS Appl. Mater. Interfaces* **2023**, *15*, 49468.
- [36] J.-J. Ryu, C.-H. Jang, *Biotechnol. Appl. Biochem.* **2023**, *70*, 1972.
- [37] N. U. Amin, H. M. Siddiqi, Y. Kun Lin, Z. Hussain, N. Majeed, *Sensors* **2020**, *20*, 298.
- [38] X. Yang, H. Li, X. Zhao, W. Liao, C. X. Zhang, Z. Yang, *Chem. Commun.* **2020**, *56*, 5441.
- [39] S. A. Oladepo, *Molecules* **2022**, *27*, 1453.
- [40] A. Concellón, D. Fong, T. M. Swager, *J. Am. Chem. Soc.* **2021**, *143*, 9177.
- [41] J. Prakash, A. Parveen, Y. K. Mishra, A. Kaushik, *Biosens. Bioelectron.* **2020**, *168*, 112562.
- [42] S. Yang, Y. Liu, H. Tan, C. Wu, Z. Wu, G. Shen, R. Yu, *Chem. Commun.* **2012**, *48*, 2861.
- [43] X. Wang, H. Wang, Y. Sun, Z. Liu, N. Wang, *Talanta* **2024**, *266*, 125025.
- [44] L. K. Gangwar, V. Sharma, A. Choudhary, G. Sumana, S. S. Pandey, H. Tanaka, A. M. Biradar, Rajesh, *J. Mol. Liq.* **2023**, *380*, 121754.
- [45] S. Liao, Y. Qiao, W. Han, Z. Xie, Z. Wu, G. Shen, R. Yu, *Anal. Chem.* **2012**, *84*, 45.
- [46] O. Yavas, M. Svedendahl, P. Dobosz, V. Sanz, R. Quidant, *Nano Lett.* **2017**, *17*, 4421.
- [47] E. Pennacchietti, C. D'Alonzo, L. Freddi, A. Occhialini, D. De Biase, *Front. Microbiol.* **2018**, *9*, 2869.
- [48] D. De Biase, A. Tramonti, F. Bossa, P. Visca, *Mol. Microbiol.* **1999**, *32*, 1198.
- [49] M. R. Wilmes-Riesenberg, B. Bearson, J. W. Foster, R. Curtis, *Infect. Immun.* **1996**, *64*, 1085.
- [50] L. P. Jones, in *Handbook of Visual Display Technology*, (Eds: J. Chen, W. Cranton, M. Fihn) Springer, Berlin, **2012**, pp. 1387–1402.
- [51] D. S. Miller, R. J. Carlton, P. C. Mushenheim, N. L. Abbott, *Langmuir* **2013**, *29*, 3154.
- [52] K. Seo, H. Kang, *Polymers* **2021**, *13*, 2058.
- [53] Q. Wang, H. Chen, H. Xing, Y. Deng, Z.-W. Luo, H.-L. Xie, *Crystals* **2021**, *11*, 418.
- [54] L. Lucchetti, T. P. Fraccia, F. Ciciulla, T. Bellini, *Sci. Rep.* **2017**, *7*, 4959.
- [55] C. E. Alupoaei, L. H. García-Rubio, *Biotechnol. Bioeng.* **2004**, *86*, 163.
- [56] J. Kiefer, N. Ebel, E. Schlücker, A. Leipertz, *Anal. Methods* **2010**, *2*, 123.